

AD-A091 169

SRI INTERNATIONAL MENLO PARK CA  
SPECTRAL CHARACTERISTICS OF MEDIUM-SCALE EQUATORIAL F-REGION IR--ETC(U)  
MAR 80 R C LIVINGSTON, C L RINO

F/G 4/1

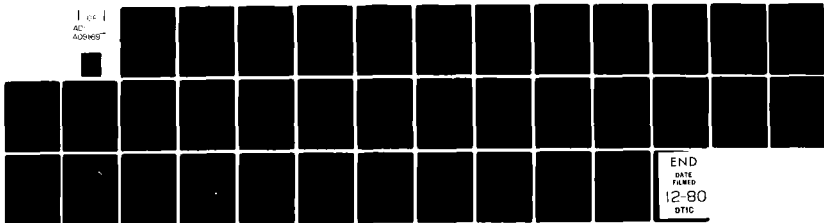
DNA001-80-C-0077

NL

UNCLASSIFIED

DNA-5311T

1 of 1  
AD  
A091169



END  
DATE  
FILMED  
12-80  
DTIC

**LEVEL**

**(12)**

**DNA 5311T**

# **SPECTRAL CHARACTERISTICS OF MEDIUM-SCALE EQUATORIAL F-REGION IRREGULARITIES**

**AD A091169**

Robert C. Livingston  
Charles L. Rino  
SRI International  
333 Ravenswood Avenue  
Menlo Park, California 94025

**DTIC  
ELECTE  
NOV 3 1980**

1 March 1980

Topical Report for Period 1 January 1980—29 February 1980

CONTRACT No. DNA 001-80-C-0077

APPROVED FOR PUBLIC RELEASE;  
DISTRIBUTION UNLIMITED.

THIS WORK SPONSORED BY THE DEFENSE NUCLEAR AGENCY  
UNDER RDT&E RMSS CODE 8322080462 125AAXHX64017 H2590D.

**DCC FILE COPY.**

Prepared for  
Director  
DEFENSE NUCLEAR AGENCY  
Washington, D. C. 20305

**80 10 24 008**

Destroy this report when it is no longer  
needed. Do not return to sender.

PLEASE NOTIFY THE DEFENSE NUCLEAR AGENCY,  
ATTN: STTI, WASHINGTON, D.C. 20305, IF  
YOUR ADDRESS IS INCORRECT, IF YOU WISH TO  
BE DELETED FROM THE DISTRIBUTION LIST, OR  
IF THE ADDRESSEE IS NO LONGER EMPLOYED BY  
YOUR ORGANIZATION.



UNCLASSIFIED

SECURITY CLASSIFICATION OF THIS PAGE (When Data Entered)

REPORT DOCUMENTATION PAGE		READ INSTRUCTIONS BEFORE COMPLETING FORM	
1. REPORT NUMBER DNA 5311T ✓	2. GOVT ACCESSION NO. AD-A091 169	3. RECIPIENT'S CATALOG NUMBER 9	
4. TITLE (and Subtitle) SPECTRAL CHARACTERISTICS OF MEDIUM-SCALE EQUATORIAL F-REGION IRREGULARITIES		5. TYPE OF REPORT & PERIOD COVERED Topical Report, for Period 1 Jan 80 - 29 Feb 80	
7. AUTHOR Robert C. Livingston Charles L. Rino		6. PERFORMING ORG. REPORT NUMBER SRI Project 1284	
9. PERFORMING ORGANIZATION NAME AND ADDRESS SRI International 333 Ravenswood Avenue Menlo Park, California 94025		8. CONTRACT OR GRANT NUMBER(s) DNA 001-80-C-0077 / 11	
11. CONTROLLING OFFICE NAME AND ADDRESS Director Defense Nuclear Agency Washington, D.C. 20375		10. PROGRAM ELEMENT, PROJECT, TASK AREA & WORK UNIT NUMBERS Subtask 125AAXHX640-17	
14. MONITORING AGENCY NAME & ADDRESS (if different from Controlling Office)		12. REPORT DATE 1 March 1980	
		13. NUMBER OF PAGES 38	
		15. SECURITY CLASS (of this report) UNCLASSIFIED	
		15a. DECLASSIFICATION DOWNGRADING SCHEDULE	
16. DISTRIBUTION STATEMENT of this Report Approved for public release; distribution unlimited.			
17. DISTRIBUTION STATEMENT of the Abstract Entered in Block 20, if different from Report			
18. SUPPLEMENTARY NOTES This work sponsored by the Defense Nuclear Agency under RDT&E RMSS Code B-22030462 125AAXHX64017 H2590D.			
19. SUBJECT TERMS (and/or keywords) (if necessary, include block numbers) Equatorial Spread F Radiowave Scintillation			
20. ABSTRACT (and/or summary) (if necessary, include block numbers) The spectral characteristics of equatorial F-region irregularities with scale sizes from a few kilometers to several hundred kilometers have been measured using data from the Atmospheric Explorer-E (AE-E) satellite. The spectra admit the expected power-law characterization with a mean spectral index slightly less than 2. The spectral index, $p$ , however, decreases with in- creasing perturbation strength.			

DD FORM 1473

UNCLASSIFIED

SECURITY CLASSIFICATION OF THIS PAGE (When Data Entered)

UNCLASSIFIED

SECURITY CLASSIFICATION OF THIS PAGE(When Data Entered)

20. ABSTRACT (Continued)

These same data have been compared with nearly simultaneous phase scintillation data from the Wideband satellite. The power-law index of the phase scintillation data varies with perturbation strength in exactly the same manner as does  $p_1$ . With realistic propagation model parameters, the scintillation-inferred perturbation levels can be made to match those measured in-situ. However, the long-accepted unity separation between the in-situ and phase spectral indices is not observed. This discrepancy is attributed either to shortcomings in the theory or to lack of temporal/spatial comparability of the two measurements.

Accession	
NTIS	
DTIC	
Unann	
Just	
By	
Distr	
Avail	
Dist	

**A**

UNCLASSIFIED

SECURITY CLASSIFICATION OF THIS PAGE(When Data Entered)

## SUMMARY

Radiowave scintillation has been a continuing concern for DNA because of its adverse effects on transionospheric communications in both natural and nuclear-disturbed environments. The Wideband satellite experiment was designed to, and already has, clarified several aspects of both the morphology and the propagation channel characteristics of ionospheric scintillation.

One of the specific objectives of the Wideband experiment has been to establish the connection between ionospheric density irregularities and the radiowave scintillation that they produce. The theory predicts that in a power-law environment the phase scintillation spectrum is a direct two-dimensional mapping of the three-dimensional irregularity spectrum, but this has never been effectively demonstrated. With this goal in mind, an analysis of in-situ data from the AE-E satellite has been carried out in a manner consistent with the Wideband analysis. These data provide an unambiguous one-dimensional measure of the medium scale density irregularities during strongly disturbed, nighttime equatorial spread-F conditions.

The analysis has verified the power law form of the in-situ density spectrum, with an average spectral index close to that measured by other experimenters. In addition to this expected behavior, however, we have found an apparently new result: a systematic decrease in the power-law slope with increasing turbulence level. This dependency of the slope on perturbation level of the in-situ irregularity spectrum has important ramifications both for nuclear phenomenology and propagation prediction.

A similar decline of phase spectral index with increasing disturbance has been observed for some time in the Wideband data, but had previously been attributed to diffraction effects. Now, the effect seems to reflect a true in-situ characteristic. In fact, the phase spectral indices for the same period of time as the AE-E observations show almost identical behavior as the density spectra.

By using a spectral approach and propagation theory based on a common turbulent strength parameter, the one-dimensional in-situ and two-dimensional phase spectra can be related. In practice, however, the very different orbits of the two satellites make such comparisons difficult. Nonetheless, the in-situ turbulence levels are consistent with those inferred from the Wideband data.

## PREFACE

The authors gratefully acknowledge the assistance of Drs. William Hanson and J. P. McClure of the University of Texas at Dallas, in the selection and interpretation of the AE-E data.

This work was sponsored by the Defense Nuclear Agency under RDT&E RMSS Code B322080462 I25AAXHX64017 H2590D.



## TABLE OF CONTENTS

SUMMARY . . . . .	1
PREFACE . . . . .	3
LIST OF ILLUSTRATIONS . . . . .	5
I    INTRODUCTION . . . . .	7
II   IN-SITU ANALYSIS AND RESULTS . . . . .	9
III  SCINTILLATION ANALYSIS AND RESULTS . . . . .	21
IV   DISCUSSION . . . . .	29
REFERENCES . . . . .	31

# LIST OF ILLUSTRATIONS

1	Comparative Spatial Scales of AE-E and Wideband Measurements. . . . .	8
2	Typical AE-E Pass, Orbit 15058, 372-km Altitude . . . . .	10
3	AE-E Density Spectra for Two Different Detrend Cutoff Frequencies. . . . .	13
4	Local Time Variation, AE-E Data . . . . .	14
5	Distribution of Observed Spectral Slopes, In-Situ Density Data. . . . .	15
6	Observed Spectral Slope vs. Spectral Strength, In-Situ Density Data. . . . .	16
7	Log RMS In-Situ Density Perturbation vs. In-Situ Spectral Strength . . . . .	17
8	In-Situ Measured Three-Dimensional Turbulent Strength. . . . .	20
9	Wideband Phase Spectral Slope vs. $S_i$ Intensity Scintillation Index at 137 and 378 MHz. . . . .	23
10	Distributions of Wideband Phase Scintillation Data, 137 MHz . . . . .	24
11	Phase Spectral Slope vs. Spectral Strength T at 137 MHz . . . . .	25
12	Scintillation Measured Three-Dimensional Turbulent Strength. . . . .	27
13	Comparison of AE-E One-Dimensional and Wideband Two-Dimensional Spectral Slopes vs. Three-Dimensional Turbulent Strength. . . . .	29

## I INTRODUCTION

Electron density irregularities in the ionosphere are observed over a vast range of spatial scales. At one extreme are the thousands-of-kilometer scale perturbations associated with tidal motions and planetary-scale waves. At the other are meter scale irregularities presumably associated with diffusive (ion gyroradius) or electrostatic (drift wave) mechanisms. Between these limits, and extending over at least three orders of magnitude in scale size, is a spatial scale regime over which the irregularity size distribution can be characterized as power law [Rufenach, 1972; Dyson et al., 1974; Phelps and Sagalyn, 1976; Crane, 1976; McClure et al., 1977; Fremouw et al., 1978].

In this report we consider the central portion of this irregularity power-law regime--the kilometer through hundreds-of-kilometer portion, as measured by two quite different methods. One measurement is a one-dimensional sampling of the irregularity structure: low spatial resolution in-situ density from the Atmospheric Explorer-E satellite (AE-E). The second measurement is two-dimensional: multifrequency scintillation from the DNA Wideband satellite. The spectral range of the in-situ data corresponds to scale sizes larger than a few kilometers, which overlaps the low frequency end of the Wideband phase scintillation spectrum as illustrated in Figure 1.

Two weeks of data are analyzed from a period for which AE-E was over Kwajalein Atoll in the equatorial Pacific, at times roughly coincident with the Wideband observations. The measurements correspond to a local time and season when the irregularity onset and evolution are dominated by the Rayleigh-Taylor instability (see Ossakow [1979] and the references cited therein).

In Section II, the in-situ data are first characterized in terms of the spectral density function (SDF) of density fluctuation. Using a three-dimensional spectral model and generalized geometry and anisotropy,

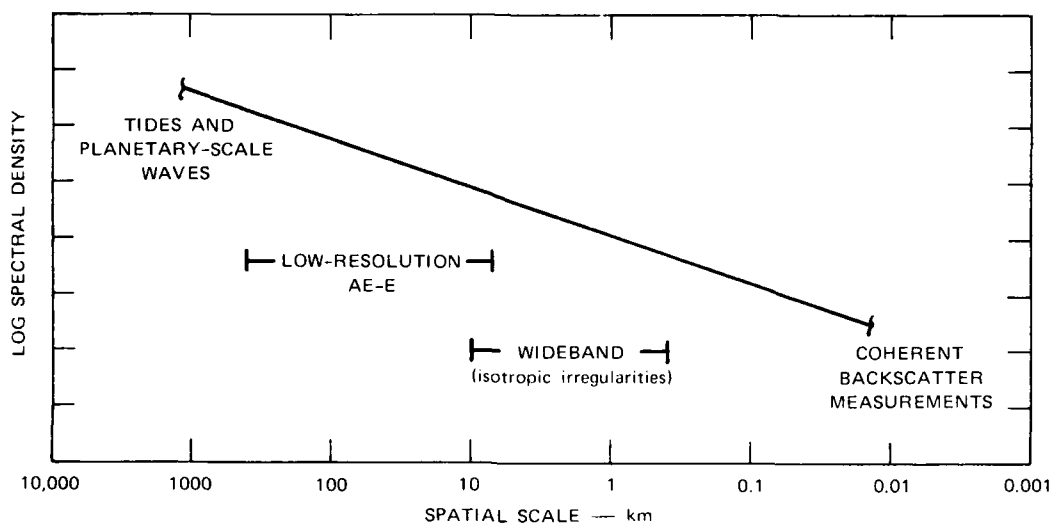


FIGURE 1 COMPARATIVE SPATIAL SCALES OF AE-E AND WIDEBAND MEASUREMENTS

the measured perturbation strengths are related to their corresponding three-dimensional turbulence strengths. In Section III, the same approach is taken with the scintillation data so that the results of two methods of measurement can be compared.

The most important finding from these data is a systematic variation of the power-law spectral index. From the AE-E data, the median value of the spectral index is slightly less than 2. However, the spectral index varies monotonically from values larger than 2 to values significantly smaller than 2 as the perturbation strength increases. A similar trend is present in the spectral index of the Wideband satellite phase scintillation data.

## II IN-SITU ANALYSIS AND RESULTS

During late July and early August 1978 the AE-E satellite was activated over Kwajalein Island ( $9^{\circ}24'N$ ,  $167^{\circ}28'E$ ) for a number of nighttime orbits. The data that follow are from the thirteen of those passes that encountered significant ionospheric disturbance. These observations were made from 0800 UT to 1400 UT or 2000 LT to 0200 LT.

Among the instruments aboard AE-E is the ion drift meter described by Hanson and Heelis [1975], from which angle-of-arrival information can be gleaned (for example, McClure et al., 1977). Also available from the drift meter is log ion density--the data we have used in this study. The spacecraft system loses some log density data each fraction of a second during drift measurements. This loss of data produces a complicated pattern of missing points; however, by interpolating over a span of only approximately  $1/50$  s, it is possible to produce a record of log ion density with an effective 3-Hz sample rate. At the satellite velocity of  $\sim 7.7$  km/s, this velocity corresponds to a sample every  $\sim 2.6$  km along the satellite path. By comparison, the high spatial resolution data from the retarding potential analyzer (e.g., McClure et al., 1977) are sampled at  $\sim 30$  m.

Figure 2(a) is a sample of the log density data over Kwajalein. For this particular pass, and for most of those during the two-week period, the satellite was below the F-region peak, as observed on ionogram records, at an altitude of 372 km. This record, which shows the signatures of distinct, isolated plasma bubbles, is typical of the AE-E data for the more strongly disturbed nights during the Kwajalein scintillation season. Coordinated measurements between AE-E and the Kwajalein radar using one of the current data sets has shown that the in-situ bubbles correspond to 1-m backscatter plumes [Tsunoda, 1980].

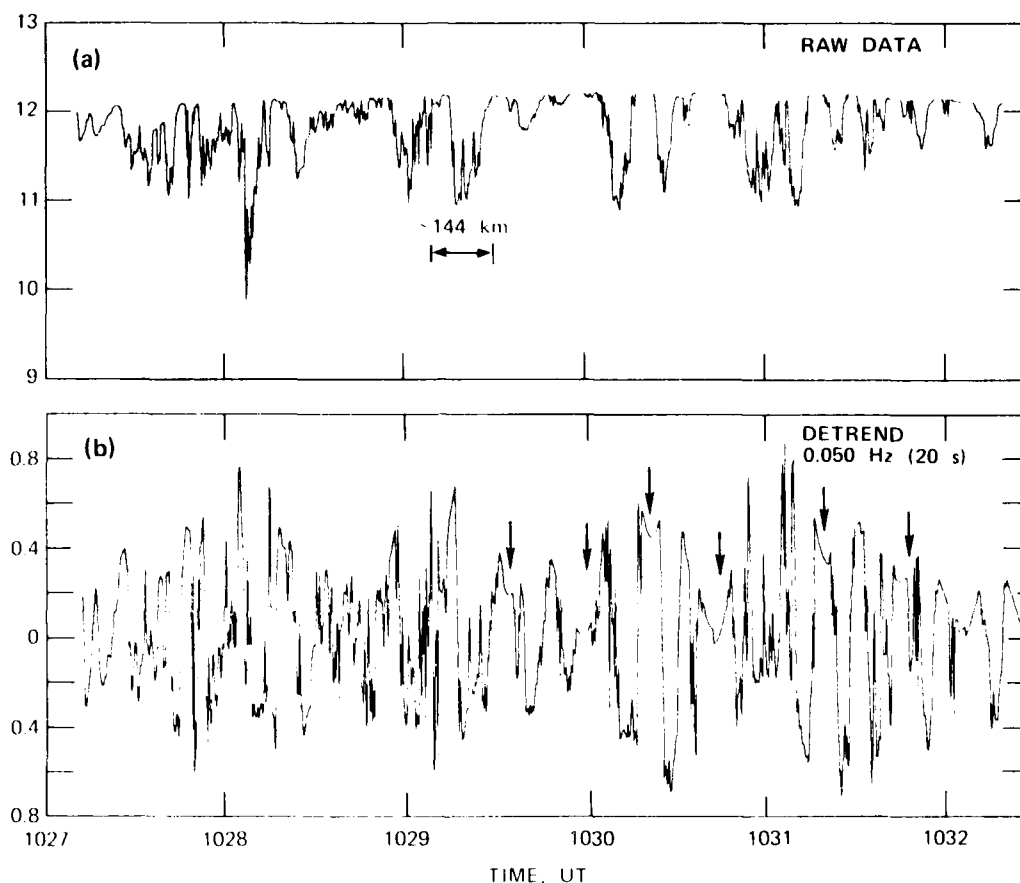


FIGURE 2 TYPICAL AE-E PASS, ORBIT 15058, 372-km ALTITUDE. (a) Raw log density and (b) Detrended linear density.

We wish to characterize these in-situ data by the SDF of their density perturbations. Before spectral analysis can be done, however, it is necessary to separate the perturbation components from the slow changes in background ion density. We have done this by using a sharp-cutoff filter, a method which has been well proven in the analysis of scintillation data. The use of a filter has the advantage over polynomial

detrending in that precisely where in frequency and how much the SDF is being affected by the process are known. In practice the data are converted to linear electron density and low-pass filtered with subsequent subtraction of the smoothed component from the original data.

The detrend cutoff frequency must be low enough to provide an adequate range for determining spectral slope, yet high enough to truly separate density trends from perturbations. A 0.02-Hz or a spatial scale cutoff of roughly 400 km has been used in the routine numerical accumulations. The same data shown in Figure 2(a) has been detrended at 0.05 Hz in Figure 2(b). Subsequent processing consists of the Fast Fourier Transform (FFT) calculation of the SDF of the detrended density perturbations and extraction of the spectral strength and slope. The spectra are calculated over a time span of about 85 s. This provides adequate spectral resolution between spatial scales from about 5 km to 600 km, and generally assures stationarity at the detrend filter cutoffs of interest. In accumulating the statistics, each span overlapped adjacent spans. Finally, spectral fits to the functional form

$$\phi(f) = T_1 f^{-p_1} \quad (1)$$

are made by calculating the least squares fit to the smoothed, log-log SDF between 0.1 Hz and 0.7 Hz, which is well above the detrend cutoff, yet below the noise floor frequency for a disturbed record. Using the least squares method forces consistency in a large number of spectral fits that cannot be obtained by eye.

Of concern in the detrending process is the detrend filter response to the rapid density changes between the bubble walls and the quiet background layer. Several of these transition regions are indicated by arrows in Figure 2(b). The degree of ringing at these transitions depends upon the filter cutoff frequency--becoming worse as the filter narrows. To verify that this energy does not contaminate the in-situ spectra in the slope-fit region, a number of spectra at various filter cutoffs have been compared. An example of those comparisons, for a data span in which

the transitions are particularly conspicuous, is shown in Figure 3 for cutoffs of 0.01 Hz and 0.05 Hz. At the low-frequency end the detrend cutoff is conspicuous, but otherwise only details of the spectra have changed. In the fit region the spectra are virtually unchanged, differing in slope fits by only a few percent. Thus, we feel that the effect of abrupt transitions on the summary statistics are negligible.

Note that the longer period detrend spectrum shows no tendency to flatten at its lowest frequencies. This indicates that if a systematic outer-scale structure size is in the density data, it is well beyond 400 km (0.02 Hz).

The mix of quiet and disturbed regions in the density data produces a broad range of spectral strength  $T_1$ , varying over more than 60 dB. To avoid the more weakly disturbed data for which the spectral slopes,  $p_1$ , may decrease by intersection with the noise floor, we have rejected data for which  $T_1 < 195$  dB.

The local time at Kwajalein for these AE-E passes ranges between 2000 LT and 0200 LT. When plotted as a function of time [Figure 4(a)], the  $T_1$  values show a systematic decline through and beyond local midnight. This systematic decline is the general trend expected in the nighttime equatorial ionosphere from scintillation and rocket measurements. Note, however, that these disturbance levels in the medium-to-large scale regime are still strong at 0200 LT despite the general disappearance of 1-m backscatter two to three hours earlier. The systematic decline of spectral strength with local time raises the question whether it is due simply to the decline in the background density. In Figure 4(b) the rms normalized perturbation,  $(\Delta N/N)^{2,1/2}$ , is plotted versus time, and also shows a systematic decrease throughout the evening. Therefore, we can attribute the observed decline in spectral slope to a true decline in the degree of turbulence over the observing window.

The second parameter that characterizes the irregularity spectra is the slope  $p_1$  [Eq. (1)] for which the distribution is shown in Figure 5. The distribution of slopes centers about  $p_1 = 1.9$  and is skewed somewhat toward even shallower values. This mean value is very close to that



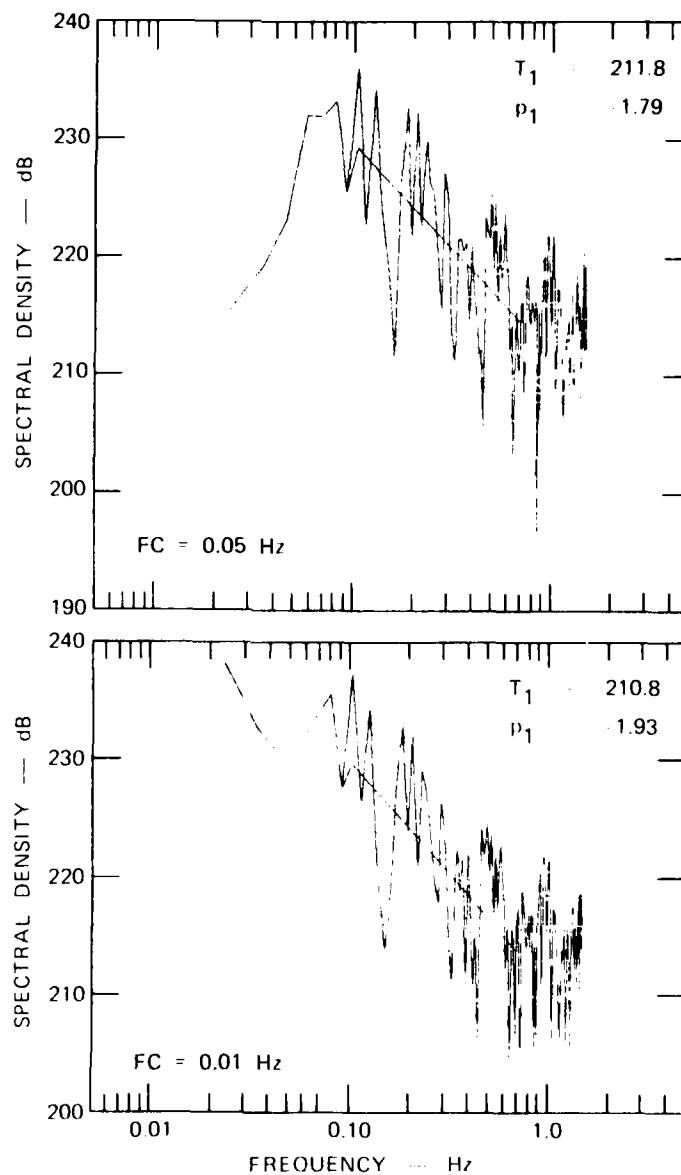


FIGURE 3 AE-E DENSITY SPECTRA FOR TWO DIFFERENT DETREND CUTOFF FREQUENCIES

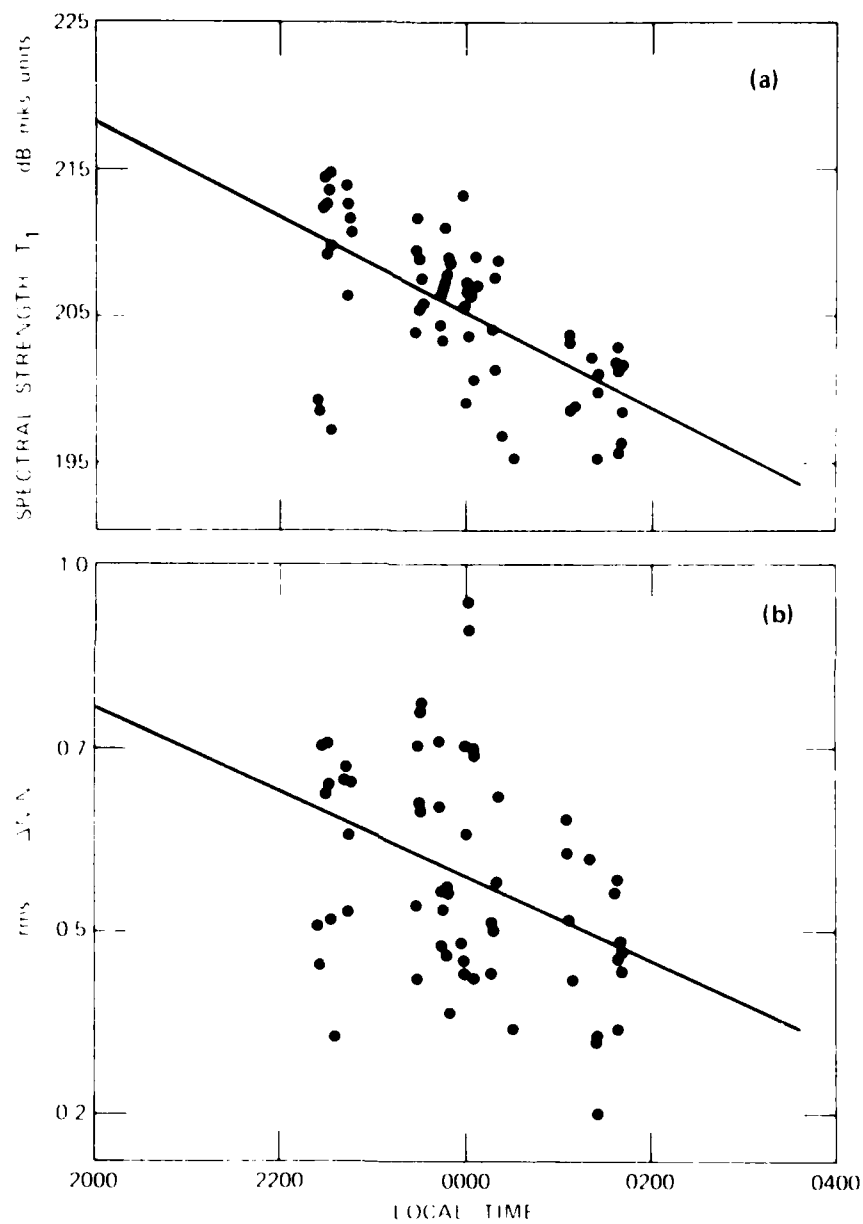


FIGURE 4 LOCAL TIME VARIATION, AE-E DATA. (a) Spectral strength  $T_1$  and (b) rms  $\Delta N/N$

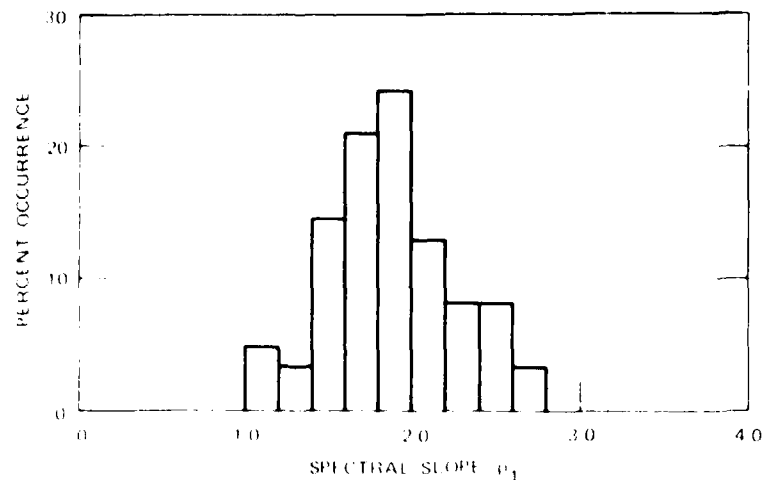


FIGURE 5. DISTRIBUTION OF OBSERVED SPECTRAL SLOPES, IN-SITU DENSITY DATA

and  $\sigma_{\rho} = 0.001$  g/cm<sup>3</sup>, or  $1.8 \times 10^{-4}$  using high resolution measurements from the Orbiting Geophysical Observatory (OGO) satellite. However, a quite different perspective on the slope distribution is obtained by plotting the spectral strength,  $I_p$ , as in Figure 6, i.e., then, as a function of the spectral slope with increasing disturbance level. This result is somewhat surprising because the theoretical model predicts that the Rayleigh-Taylor instability, when driven by stratification, produces steep gradient and a corresponding "broad" spectral peak. This point will be further discussed in connection with the interaction with scintillation in later.

Further indication of a nonconstant spectral slope is shown in Figure 7 in which the  $\chi^2$  perturbation,  $(\chi^2/N)^{1/2} I_p^{-1/2}$ , is plotted against spectral strength,  $I_p$ . The perturbation variance is simply an integration of the power spectrum, and if the spectral slope,  $p_1$ , is constant, the relationship between  $(\chi^2/N)^{1/2} I_p^{-1/2}$  and  $I_p$  depends only on the integration

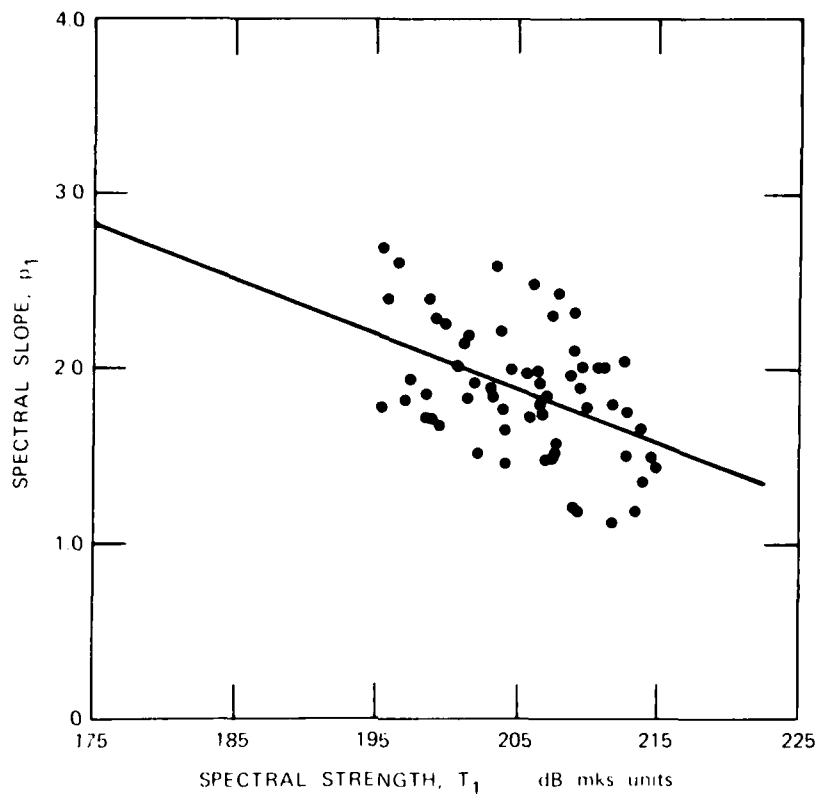


FIGURE 6 OBSERVED SPECTRAL SLOPE vs. SPECTRAL STRENGTH, IN-SITU DENSITY DATA

interval. In our case, a sampling rate of 3 Hz implies a functional dependence indicated by the dashed line in Figure 7, which differs from the observed dependence. On the other hand, the high correlation between  $(\Delta N)^2)^{1/2}$  and  $T_1$  reassures the validity of the characterization of the spectra in terms of  $T_1$  and  $p_1$ .

Up to this point we have dealt with the two measurable parameters,  $T_1$  and  $p_1$ , which characterize the temporal SDF of the in-situ density perturbation. We now wish to consider the conversion of those data to a spatial parameter that can be generally compared to other measures of turbulence, and, in particular, to the scintillation data of the next section.

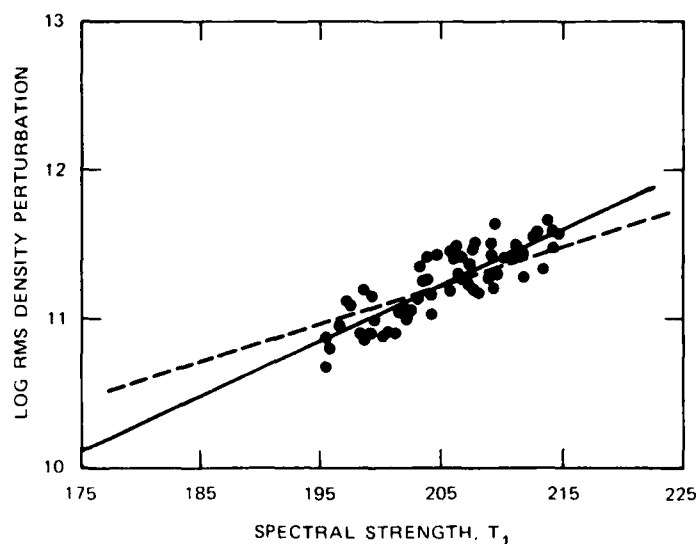


FIGURE 7 LOG RMS IN-SITU DENSITY PERTURBATION vs. IN-SITU SPECTRAL STRENGTH. The dashed line indicates predicted correlation for constant spectral slope.

In the general case, the time-space conversion of the in-situ data involves both the direction of the spacecraft and the irregularity anisotropy. This can be shown starting from an appropriate functional form of the three-dimensional fluctuation spectrum, e.g., the general form for the power-law SDF in three dimensions of Rino and Fremouw [1977]. Because we are investigating a spatial regime well above the inner scale, we have chosen the simplification of that model used by Rino [1979].

Rino [1979] retains generalized anisotropy, and geometry; he describes the three-dimensional fluctuation SDF as

$$f_{\perp N}(q) = abC_s q^{-(2\nu+1)} \quad (2)$$

when no outer scale cutoff is assumed. The terms,  $a$  and  $b$ , describe the anisotropy of the density irregularities and are the axial ratios along and across the magnetic field, respectively.

$$C_s = 8\pi^{3/2} / (LN^2) q_0^{2\nu-2} \Gamma(\nu + 1/2) / \Gamma(\nu - 1) \quad (3)$$

is the strength of the three-dimensional in-situ turbulence dependent upon the outer scale wave number,  $q_0$ , and the slope parameter,  $\nu$ .

As Rino [1979] indicated, the three dimensional autocorrelation function that follows from Eq. (2) is

$$R_{N_c}(y) = \frac{C_s}{q_0^{3/2} \Gamma(\nu + 1/2)} \left| \frac{y}{2q_0} \right|^{\nu-1} K_{\nu-1}(q_0 y) \quad (4)$$

Further transformation of Eq. (4) with the spatial variable replaced by velocity-time product yields the one-dimensional temporal SDF as an in-situ probe would measure it:

$$\chi_p(t) = \frac{C_s \Gamma(\nu + 1/2)}{q_0^{3/2} \Gamma(\nu + 1/2)} \frac{1}{v_p \left( q_0^2 + (2.1t/v_p)^2 \right)^{\nu + 1/2}} \quad (5)$$

the cross-field speed,  $v_p$ , is dependent upon both the probe velocity and the irregularity anisotropy. From Rino [1979], the form of  $v_p$  is

$$v_p^2 = v^2 \underline{C}^T \quad (6)$$

where  $v$  is the probe velocity and the matrix,  $\underline{C}$ , is derived from the generalized irregularity model that Rino and Fremouw [1977] discuss. It will suffice to say that for rod-like, field-aligned irregularities of a field ratio,  $\alpha$ , the off-diagonal terms of  $\underline{C}$  are zero. Furthermore, for isotropic irregularities ( $\alpha = 1$ ) the three diagonal terms are unity, so that  $v_p$  is simply the probe speed.

At a point well-represented by the outer scale cutoff, Eq. (5) can be written in a form analogous to Eq. (1), used to characterize the one-dimensional SDF:

$$\chi_p(t) = \Gamma_1 t^{-(2\nu-1)} \quad (7)$$

$$T_1 = \frac{C_s \Gamma(\nu - 1/2)}{4\pi^2 \Gamma(\nu + 1/2)} \frac{1}{v_p (2\pi/v_p)^{2\nu-1}} \quad (8)$$

Note from Eq. (7) that the slope parameters relate as

$$\nu = \frac{p_1 + 1}{2} \quad (9)$$

Eqs. (7) and (8) concisely relate the temporal SDF measurables,  $T_1$  and  $p_1$ , to the three-dimensional spatial turbulence level for generalized anisotropy and geometry. In applying the measured spectral characteristics to calculate the strength of turbulence via Eqs. (7) and (8), we have chosen to use the measured values of spectral strength  $T_1$  with a functional dependence of slope,  $p_1(\log T_1)$ , based on the least squares fit illustrated in Figure 6. The resulting distribution of  $C_s$ , based on the in-situ measurements, is shown in Figure 8(a). The distribution is broadened from that of  $T_1$ , primarily from the nonconstant slope which has been used, and secondarily from the variation in satellite direction, and, therefore,  $v_p$  from orbit to orbit.

More instructive is the dependence of spectral slope,  $p_1$ , on  $C_s$  as shown in Figure 8(b). The decrease of spectral slope with increasing turbulence strength is again clear; there is an overall decrease of about unity slope between 2.5 and 1.5 over about 60 dB of increase in  $C_s$ . Because the direction of AE-E is primarily magnetic west-east at Kwajalein, Figure 8(b) changes little with the choice of anisotropy model. From isotropic to 1000:1 or even nonrod models, the  $C_s$  values change by only a few percent, and the dependence of slope upon  $C_s$  indicated by the least squares fit remains virtually unchanged.

To summarize the in-situ data, we observe a decrease in the degree of turbulence with time over the evening hours from 2000 LT to 0200 LT. The spectral index of the density perturbations show an arithmetic mean very close to that observed by others. When we plot the spectral index a function of spectral strength of three-dimensional turbulence, however, we observe a systematic decrease in spectral slope with increasing turbulence.

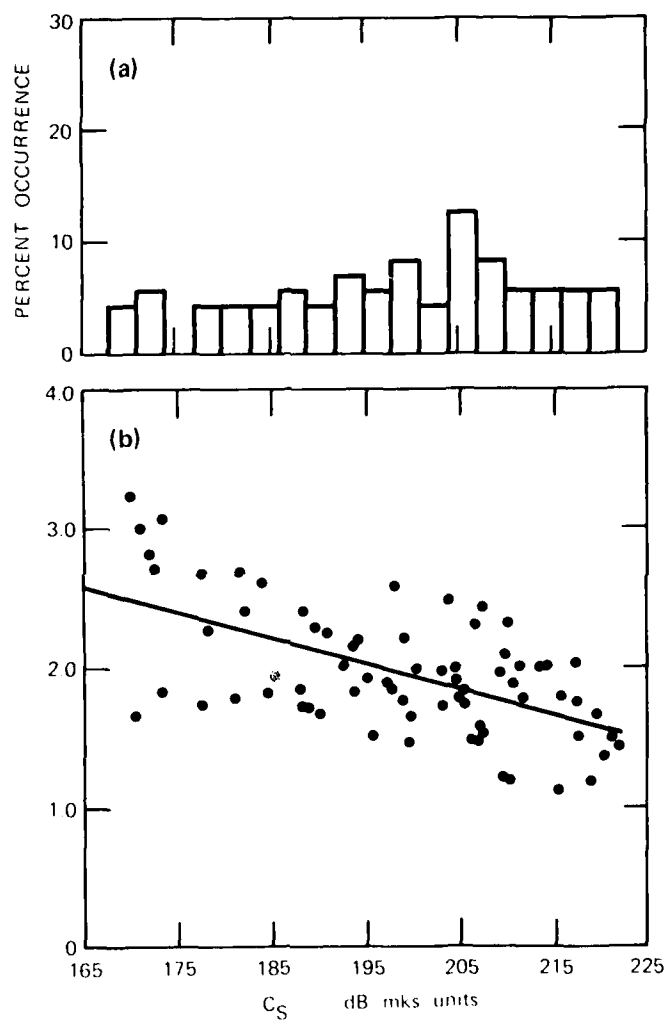


FIGURE 8 IN-SITU MEASURED THREE-DIMENSIONAL TURBULENT STRENGTH.  
 (a) Distribution of  $C_S$  and (b) Spectral slope  $p_1$  vs.  $C_S$



### III SCINTILLATION ANALYSIS AND RESULTS

During the same period that the AE-E data, just described, were collected, the DNA Wideband system [Fremouw et al., 1977] was operating at Kwajalein. The scintillation season at Kwajalein is centered about local summer, and shows a considerable degree of variability from week to week. During the late-July/early-August 1978 period of interest, the overall scintillation was moderate to strong. Considerably more severe scintillation has been observed at Kwajalein during other periods [Livingston, 1980]. Of the satellite data collected daily, nine nighttime passes were disturbed and form the data base for the following discussion. These were collected between about 1130 UT and 1300 UT (1300 LT to 0100 LT), thereby overlapping the AE-E observations.

Fremouw et al. [1978] review the analysis applied to the Wideband data. In brief, the phase coherent system allows measurement of signal intensity and phase at several VHF through L-band frequencies. A sharp cutoff filter at 10 s is used to separate the rapid phase components from the slowly changing background. This scintillation component is subsequently processed in 20-s blocks. Included in this processing is the computation of phase spectral density functions at 137 MHz and 378 MHz, which are least squares fit over a selected frequency range to the form

$$S(f) = T f^{-p}, \quad (10)$$

analogous to the AE-E processing [Eq. (1)].

Rino [1979] has demonstrated and discussed the consistency of the phase spectral parameters between VHF, UHF, and L-band frequencies. In particular, he shows that  $p$  is independent of frequency, and that  $T \propto f_0^2$  when the small correction for finite reference frequency is included.

Both of these items indicate that diffraction effects are probably negligible in the phase spectra.

In Figure 9 we demonstrate that same consistency for the much smaller current data set, where  $p$  is plotted versus the  $S_4$  intensity scintillation index. Least square fits to the data are indicated for 137 MHz and 378 MHz. In general, the agreement between the slopes at the two frequencies as a function of  $S_4$  is excellent. Given this consistency, and to simplify discussion, we will present only the 137-MHz data in what follows. Similar analysis for the 378-MHz phase scintillation has produced quantitatively equivalent results.

In Figure 9, for the low  $S_4$ , weakly disturbed data, the phase slopes are flattened by intersection with the spectral noise floor. At the high  $S_4$ , stronger scatter end, the phase slopes also decline; this effect is more conspicuous in these data than in the larger data set analyzed by Rino [1979]. Rino [1979] attributed this effect to diffraction-produced, rapidly changing steep phase fronts, which drive the SDF dependence toward  $f^{-2}$ . In light of the AE-E data, however, this trend appears to reflect a consistent characteristic of the in-situ irregularities.

As was the case for the in-situ data, the patchy nature of the equatorial disturbance produces a spread distribution of the observed scintillation strength. To eliminate the weak scatter disturbances, we have sorted the data according to  $S_4$  index, eliminating points with  $S_4 < 0.4$  for which the derived phase spectral slopes may be biased by noise. With this criterion applied, we get the distributions of spectral strength  $T$  and slope  $p$  illustrated in Figure 10. The mean value of slope here is  $\sim 2.4$ , only slightly smaller than the value that Rino [1979] found. However, it is considerably lower than the nominal  $p = 3$  that Crane [1976] reported. In Figure 11 the observed phase scintillation slopes are plotted versus spectral strength to produce a counterpart to Figure 6 of the in-situ data. Here, as in the other data, we find a systematic decrease in spectral slope with increasing turbulence level.

The conversion of these data to three dimensional turbulence strength,  $C_s$ , provides a means of direct comparison to those derived in situ.

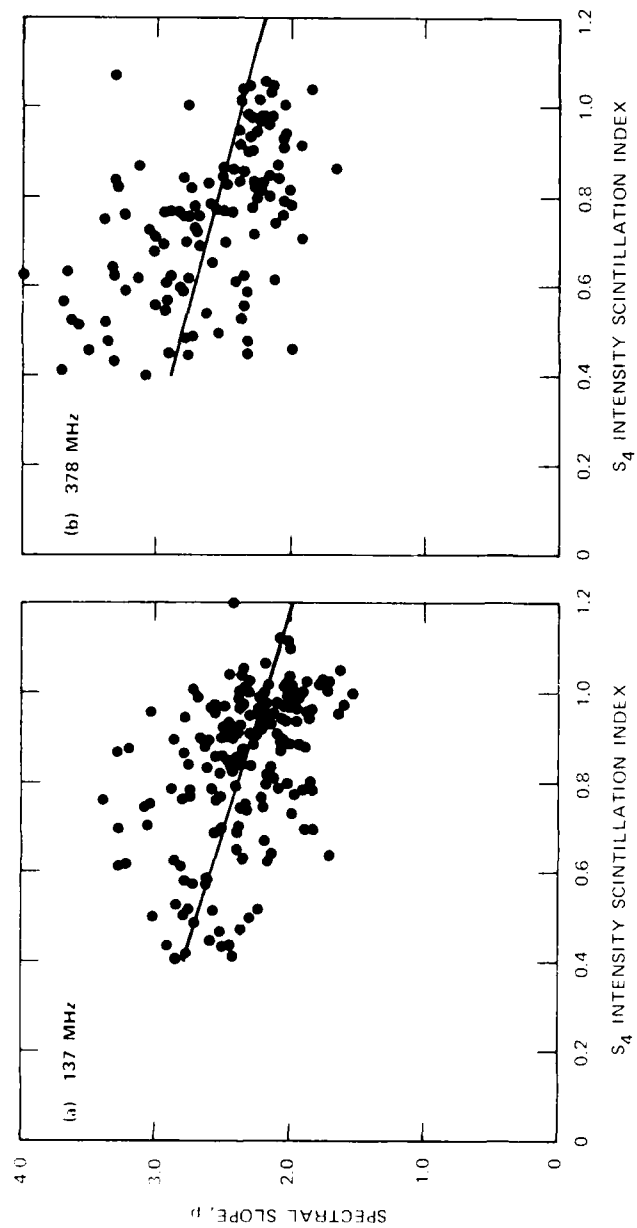


FIGURE 9 WIDEBAND PHASE SPECTRAL SLOPE vs.  $S_4$  INTENSITY SCINTILLATION INDEX AT 137 and 378 MHz

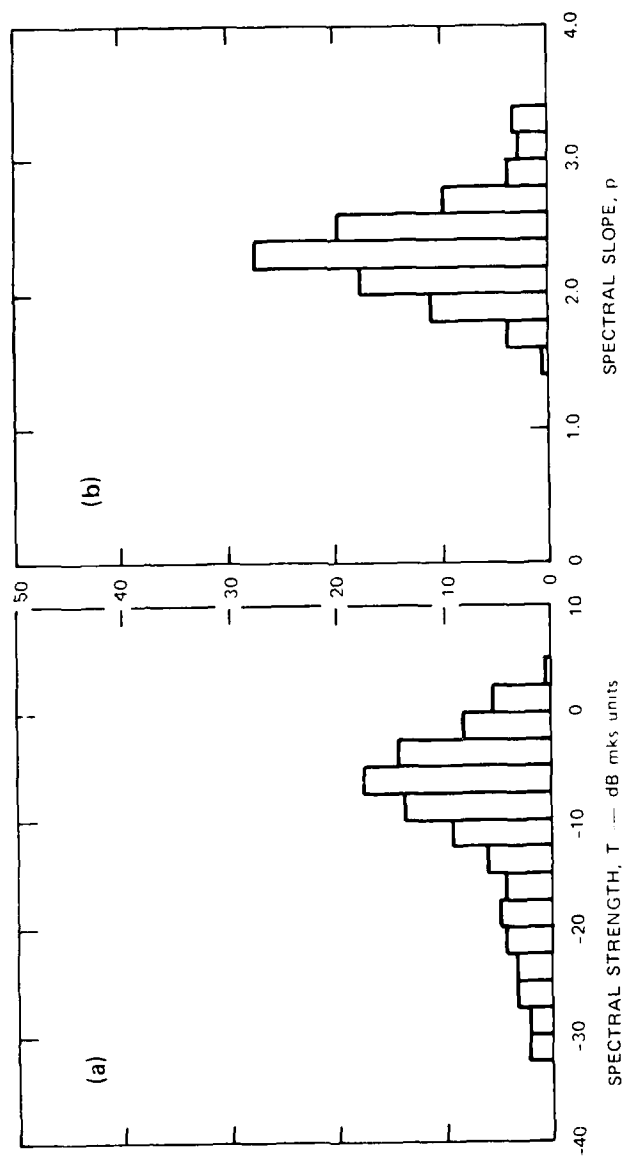


FIGURE 10 DISTRIBUTIONS OF WIDEBAND PHASE SCINTILLATION DATA, 137 MHz. (a) Spectral strength and (b) Spectral slope.

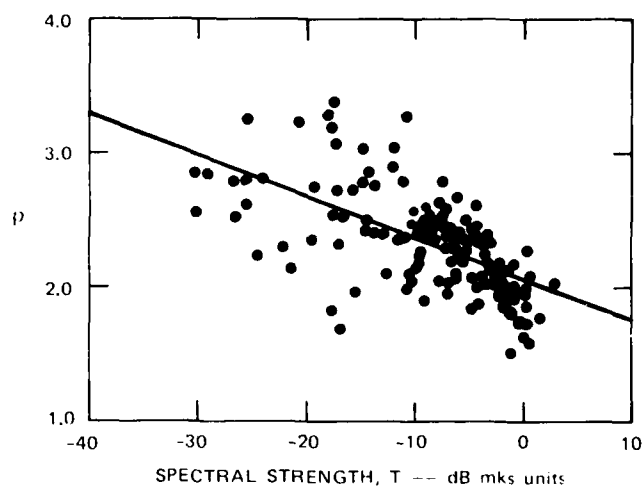


FIGURE 11 PHASE SPECTRAL SLOPE vs. SPECTRAL STRENGTH T AT 137 MHz

In the phase scintillation case, the in-situ spectral form, Eq. (2) can be related to the SDF of phase using the phase-screen model, as done by Rino [1979]. Analytically, an appropriate form for the three-dimensional autocorrelation function (ACF) is established, from which the two-dimensional temporal ACF is derived. The spatial/temporal conversion involves the relative drift of the medium across the propagation path, from source motion or irregularity drift. The resulting temporal ACF of observed phase is:

$$\psi(\tau) = \frac{T}{[t_o^2 + \tau^2]^\nu} \quad (11)$$

where  $t_o$  is the temporal outer scale defined as  $t_o = (v_{eff} q_o / 2\pi)$ , and  $T$ , the spectral strength, is defined as

$$T = r_e^2 \frac{L \sec \theta}{c} \frac{\lambda^2 \Gamma(\nu)}{(2\pi)^{2\nu+1} \Gamma(\nu + 1/2)} v_{eff}^{2\nu-1} \quad (12)$$

In Eq. (12),  $r_e$  is the classical electron radius,  $\lambda$  is the radio wavelength,  $L$  is the equivalent layer thickness, and  $\theta$  is the zenith angle

of propagation through the layer.  $G$  and  $v_{\text{eff}}$  are geometrical factors that can change throughout a Wideband satellite pass.  $G$  reflects the disturbance enhancement produced by coherent propagation, e.g., along the long axis of an extended irregularity, while  $v_{\text{eff}}$  accounts for the spatial-temporal conversion at the ionospheric penetration point. Because  $v_{\text{eff}}$  depends upon the propagation direction with respect to the principal irregularity axis, it is also highly dependent upon the chosen anisotropy model.

Rewriting Eq. (11) for frequencies well below the outer scale gives a form for the phase SDF similar to Eq. (1)

$$\varphi(f) = T f^{-2N} \quad (13)$$

Comparison with Eq. (9) shows that in the phase scintillation case,  $p = 2N$ .

In Eq. (12), therefore, we have a means to convert the measured  $T$  and  $p$  to three-dimensional turbulent strength  $C_s$ , as done with the in-situ data. As in the in-situ analysis, the measured values of  $T$  have been used to calculate  $C_s$  using an expression for slope,  $p$  ( $\log T$ ), derived from the least-squares fit of Figure 11. For initial comparisons we have assumed an equivalent 400-km thick, uniform layer centered at 300 km, and 100:1 irregularity rod model. Note, from Eq. (12), that  $C_s$  is linearly dependent upon the layer thickness  $L$ . Moreover, for the rod-like model, the irregularity anisotropy strongly affects the  $C_s$  calculation through the  $v_{\text{eff}}$  term only at low axial ratios. Beyond  $a \sim 10$  the effect saturates rapidly because of the north-south, nearly field-aligned direction of satellite travel. If we restrict ourselves then, to rod-like irregularities and realistic layer thicknesses and heights, the value of  $C_s$  can be shifted only some few dB.

The phase scintillation-implied distribution of  $C_s$  is shown in Figure 12(a). It is of roughly the same magnitude as the in-situ implied  $C_s$  data, but of quite different shape. It can be argued that the different distribution shapes are consistent with the probe and propagation

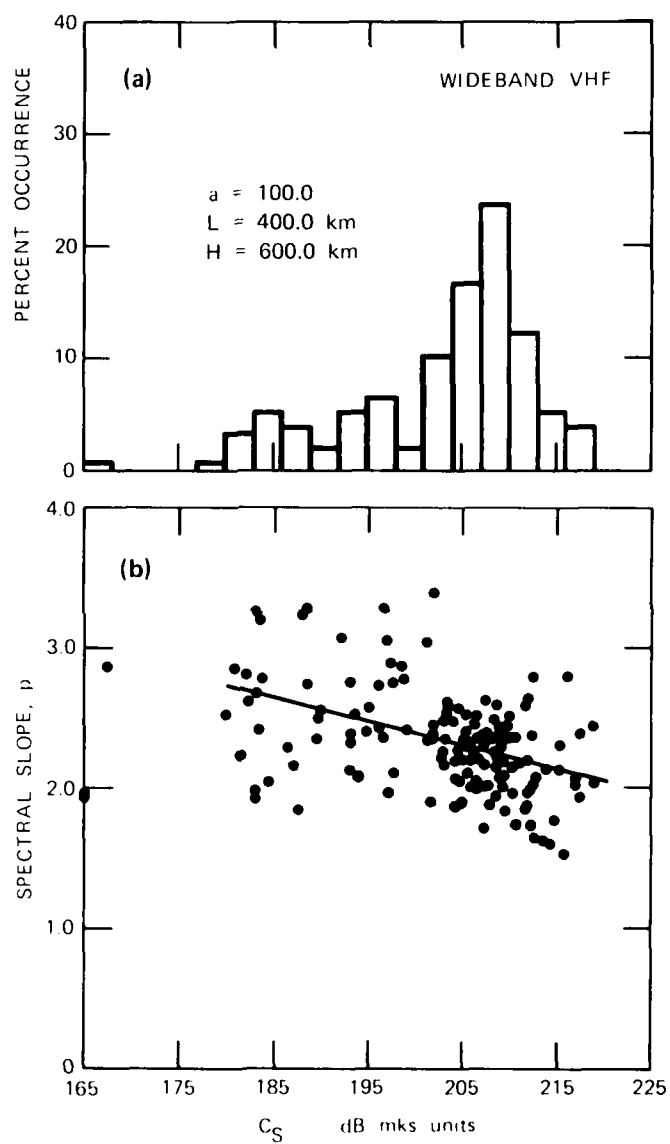


FIGURE 12 SCINTILLATION MEASURED THREE-DIMENSIONAL TURBULENT STRENGTH. (a) Distribution of  $C_S$  and (b) Spectral slope,  $p$ , vs.  $C_S$

geometries. The probe, travelling west to east, encounters multiple plumes varying in strength and internal structure. Over the thirteen orbits used here, each covering over 3000 km, an approximately uniform sampling is expected. Wideband, on the other hand, in its rapid (15 min) north-to-south scan tends to sample fewer plumes, and when it does, probes the long and more consistently structured axis of the disturbance. The conversion from T to  $C_s$  also produces Figure 12(b), in which the measured phase SDF slopes are plotted versus  $C_s$ . The decrease of  $p$  with increasing  $C_s$  is clear, as it was with the in-situ data.



#### IV DISCUSSION

The in-situ and phase scintillation perturbation strengths have been expressed in terms of  $C_s$ , a common measure from which the geometry, scale size and anisotropy dependences have been removed. In Figure 13 the least squares estimates and their rms errors from the in-situ and phase data of Figures 8 and 12 are superimposed. The slopes of the least-squares fits  $p_1(\log C_s)$  and  $p(\log C_s)$  differ only by a few percent. The agreement between these results from two very different experiments is important. It firmly demonstrates that a constant rate of decrease in the in-situ spectral index with increasing turbulence strength, is a consistent property of medium-scale spread-F irregularities.

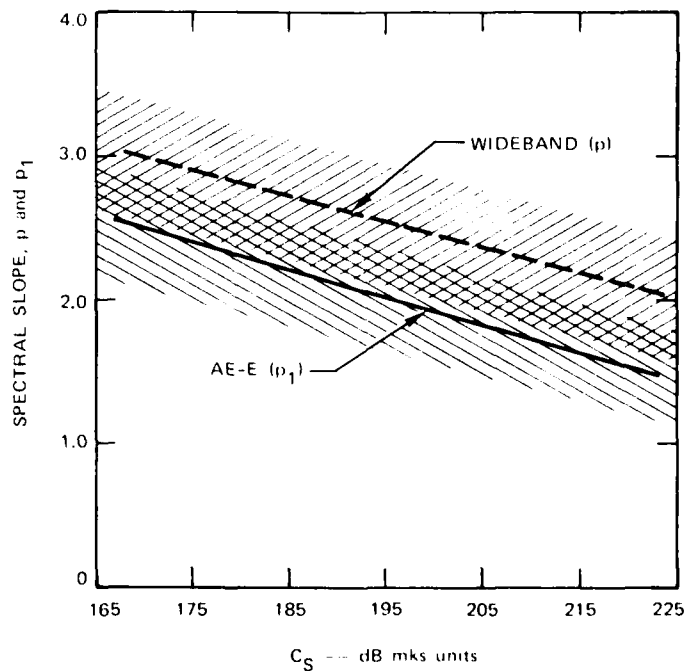


FIGURE 13 COMPARISON OF AE-F ONE-DIMENSIONAL AND WIDEBAND TWO-DIMENSIONAL SPECTRAL SLOPES vs. THREE-DIMENSIONAL TURBULENT STRENGTH

The theoretical considerations of Sections II and III indicate that the in-situ and scintillation phase slopes should differ by unity. We observe instead a consistent slope behavior for both measurements, separated by about 0.6. There are a number of reasons that may contribute to this discrepancy. An overall decrease in the phase spectral index may occur because of spatial smearing along the propagation path. Diffraction effects in phase, ignored here, may be present. Alternatively, the three-dimensional spectral model and the model parameters we have chosen can be questioned. A basic step in the long accepted theory relating the spatial autocorrelation function of density to that of phase is that the structure decorrelation scale is small compared to the contributing layer thickness. If this criterion is not satisfied, the assumption of unity separation of the phase and  $p_1 + 2$  in-situ slope may be incorrect.

It might also be argued that the in-situ and scintillation data sets, in terms of the details of these slopes, are for some reason not generally comparable. This could be a result of the very different orbital directions of the two satellites. More likely it may be due to the spatial separations in latitude, longitude and altitude between the regions probed by the two experiments. For example, although the in-situ and phase  $C_s$  distributions roughly overlay, it is conceivable that the scintillation data is dominated by more strongly perturbed and more shallowly sloped structure at altitudes not sampled by AE-E.

Resolution of these spectral slope questions may lie in the large volumes of scintillation and in-situ data which already exist. Furthermore, systematic comparisons of these larger data sets may help explain the decrease of spectral slope with the increasing level of turbulence.

## REFERENCES

- Crane, R., "Spectra of Ionospheric Scintillation," J. Geophys. Res., 81, 2041, 1976.
- Dyson, P. L., J. P. McClure, and W. B. Hanson, "In Situ Measurements of the Spectral Characteristics of F-Region Ionospheric Irregularities," J. Geophys. Res., 79, 1497, 1974.
- Fremouw, E. J., R. L. Leadabrand, R. C. Livingston, M. D. Cousins, C. L. Rino, B. C. Fair, and R. A. Long, "Early Results from the DNA Wideband Satellite Experiment--Complex-Signal Scintillation," Radio Science, 13, 167, 1978.
- Hanson, W. B. and R. A. Heelis, "Techniques for Measuring Bulk Gas-Motions from Satellites," Space Science Instrumentation, 1, 493, 1975.
- Livingston, R. C., "Comparison of Multifrequency Equatorial Scintillation: American and Pacific Sectors," Radio Science, accepted for publication, 1980.
- McClure, J. P., W. B. Hanson, and J. H. Hoffman, "Plasma Bubbles and Irregularities in the Equatorial Ionosphere," J. Geophys. Res., 82, 2650, 1977.
- Ossakow, S. L., "Ionospheric Irregularities," Rev. Geophys. Space Phys., 17, 521, 1979.
- Phelps, A. D. R. and R. C. Sagalyn, "Plasma Density Irregularities in the High-Latitude Top Side Ionosphere," J. Geophys. Res., 81, 515, 1976.
- Rino, C. L., "A Power-Law Phase Screen Model for Ionospheric Scintillation I. Weak Scatter," Radio Science, 14, 1135, 1979.
- Rino, C. L. and E. J. Fremouw, "The Angle Dependence of Singly Scattered Wavefields," J. Atmos. Terr. Phys., 39, 859, 1977.
- Rufenach, C. L., "Power-Law Wavenumber Spectrum Deduced from Ionospheric Scintillation Observations," J. Geophys. Res., 77, 4761, 1972.
- Tsunoda, R. T., "On the Spatial Relationship of 1-Meter Equatorial Spread-F Irregularities and Plasma Bubbles," J. Geophys. Res., in press, 1980.

# DISTRIBUTION LIST

## DEPARTMENT OF DEFENSE

Assistant to the Secretary of Defense  
 Main: 10000  
 ATTN: Executive Assistant

Command & Control Technical Center  
 Department of Defense  
 ATTN: 10000

Defense Advanced Research Agency  
 ATTN: 10000

Defense Communications Agency  
 ATTN: Code 10, 1. Barna  
 ATTN: Code 1010  
 ATTN: Code 100, 1. Dieter

Defense Communications Engineer Center  
 ATTN: Code 8410, 1. Traighill  
 ATTN: Code 8410, 1. McLean  
 ATTN: Code 8410

Defense Research Agency  
 ATTN: 10000  
 ATTN: 10000  
 ATTN: 10000

Defense Research & Development Center  
 ATTN: 10000

Field Command  
 Defense Research Agency  
 ATTN: 10000

Field Command  
 Defense Research Agency  
 ATTN: 10000

Interagency Research & Development  
 ATTN: 10000

Joint Research & Development  
 ATTN: 10000

Joint Research & Development  
 ATTN: 10000

Joint Research & Development  
 ATTN: 10000

Joint Research & Development  
 ATTN: 10000

Joint Research & Development  
 ATTN: 10000

Joint Research & Development  
 ATTN: 10000

## DEPARTMENT OF THE ARMY

ARM Advanced Technology Center  
 Department of the Army  
 ATTN: 10000

Army Diamond Laboratory  
 Department of the Army  
 ATTN: 10000-10, 1. M. Wether  
 ATTN: 10000-10, 1. W. Wether  
 ATTN: 10000-10

Army Command & Control Laboratory  
 ATTN: 10000-10, 1. M. Wether

Army Foreign Science & Technology  
 ATTN: 10000

Army Intelligence Command  
 ATTN: 10000

Army Intelligence Research Activity  
 ATTN: 10000

## DEPARTMENT OF THE NAVY

Naval Research & Development  
 ATTN: 10000  
 ATTN: 10000  
 ATTN: 10000

Naval Research & Development  
 ATTN: 10000

Naval Research & Development  
 ATTN: 10000

Naval Research & Development  
 ATTN: 10000  
 ATTN: 10000  
 ATTN: 10000  
 ATTN: 10000

Naval Research & Development  
 ATTN: 10000

Naval Research & Development  
 ATTN: 10000

## DEPARTMENT OF THE AIR FORCE

Air Force Research & Development  
 ATTN: 10000  
 ATTN: 10000  
 ATTN: 10000

Air Force Research & Development  
 ATTN: 10000

Air Force Research & Development  
 ATTN: 10000  
 ATTN: 10000  
 ATTN: 10000

DEPARTMENT OF THE AIR FORCE (Continued)

Air Force Wright Aeronautical Laboratories  
ATTN: A. Johnson

Ballistic Missile Office  
Air Force Systems Command  
ATTN: MNML, S. Kennedy

Foreign Technology Division  
Air Force Systems Command  
ATTN: GIL's Library

Ground Systems Force Division  
Air Force Systems Command  
ATTN: MA, M. Clavin

Space Systems Development Center  
Air Force Systems Command  
ATTN: [illegible]

Systems Development Division  
Air Force Systems Command  
ATTN: [illegible]

Systems Development Division

Systems Development Division

Systems Development Division

Systems Development Division

Systems Development Division

Systems Development Division

Systems Development Division

Systems Development Division

Systems Development Division

Systems Development Division

Systems Development Division

DEPARTMENT OF DEFENSE CONTRACTORS (Continued)

APTEK  
ATTN: T. Meagher

Berkeley Research Associates, Inc.  
ATTN: J. Workman

Boeing Co  
ATTN: D. Clauson

Charles Stark Draper Lab, Inc  
ATTN: D. Cox  
ATTN: J. Gilmore

Computer Sciences Corp  
ATTN: J. Spoor  
ATTN: C. Nail

Cornell University  
Department of Electrical Engineering  
ATTN: D. Farley, Jr.

Electrospace Systems, Inc  
ATTN: P. Phillips

EMI, Inc  
ATTN: C. Marshall  
ATTN: C. Prettie

General Electric Co  
ATTN: L. Reibert

General Electric Company—TEMP  
ATTN: W. Gump  
ATTN: D. Gump

General Research Corp  
ATTN: J. Gumbart  
ATTN: J. Gumbart

University of Illinois  
ATTN: K. Goh

Institute for Defense Analysis  
ATTN: E. Lamer

International Tel & Telegraph Corp  
ATTN: Technical Library

ITT  
ATTN: J. Gumbart

Lockheed Corporation  
ATTN: J. Gumbart

Rockwell Corp  
ATTN: J. Gumbart

Rockwell Corp  
ATTN: J. Gumbart

Rockwell Corp  
ATTN: J. Gumbart

DEPARTMENT OF DEFENSE CONTRACTORS (Continued)

Mission Research Corp

ATTN: R. Hendrick  
ATTN: F. Fajen  
ATTN: R. Kilb  
ATTN: D. Sappenfield  
ATTN: R. Bogusch

Mitre Corp

ATTN: B. Adams

Mitre Corp

Westgate Research Park

ATTN: J. Wheeler  
ATTN: W. Foster  
ATTN: W. Hall

R&D Associates

ATTN: R. Lelevier  
ATTN: W. Karzas  
ATTN: C. MacDonald  
ATTN: M. Gantsweg  
ATTN: B. Gabbard  
ATTN: P. Haas

DEPARTMENT OF DEFENSE CONTRACTORS (Continued)

Rand Corp

ATTN: E. Bedrozian  
ATTN: C. Grain

Science Applications, Inc

ATTN: D. Sachs  
ATTN: D. Hamlin  
ATTN: L. Linson

SRI International

ATTN: R. Leadabrand  
ATTN: V. Gonzales  
ATTN: R. Hake, Jr.  
ATTN: W. Chesnut  
ATTN: D. McDaniels

10 cy ATTN: C. Rino

10 cy ATTN: R. Livingston

Technology International Corp

ATTN: W. Boquist

**FILMED**  
**2-8**